Kashf Journal of Multidisciplinary Research
Vol:03 – Issue 03 (2026)
P-ISSN: 3007-1992 E-ISSN: 3007-200X
https://kjmr.com.pk

CFD ANALYSIS OF HEAT TRANSFER IN AN AIR-COOLED BATTERY THERMAL MANAGEMENT SYSTEM

Muhammad Zahid[1], Khadija Faiz[2]

[1, 2]Department of Mathematics and Statistics, University of Southern Punjab, Multan 66000, Pakistan.

[*]***Corresponding Author:***(muhammadzahid82@gmail.com)

DOI:(*https://doi.org/10.71146/kjmr862*)

Article Info

Abstract

In this study, a battery pack is under consideration for its thermal management because during operational conditions, heat is produced as a byproduct, and if not removed, the heat will damage the battery pack. That is why, we have used CFD simulations for the analysis of battery thermal management. The battery cells are exposed to the air in an inlet and outlet arrangement. Variable inlet velocity conditions have been employed to analyze its impact on the heat swept. The operating parameters is the inlet velocity for a fixed heat generation rate of 4,20,000 W/m^3 in the battery cells, while the target parameters are the heat transfer coefficient, battery temperature and the inlet pressure. The flow model is the 3D- Navier-Stokes equations along with the additional transport equations of Standard k-ϵ turbulence model. The simulations are conducted on ANSYS Workbench, while the solver is Fluent.

Keywords:

CFD, Lithium-ion cell, Thermal management, Simulation.

1. INTRODUCION

The escalating issues of air contamination, shifts in climate patterns, and rising global temperatures have underscored the urgent need to adopt sustainable energy alternatives. Within this context, the automotive sector is actively steering toward electrification, with electric vehicles emerging as a central solution. Among the array of available energy storage options, batteries stand out due to their capability to deliver strong peak and sustained power outputs efficiently [1]. Among battery technologies, lithium-ion variants have become the dominant choice, owing to advantages such as high power-to-weight ratio, superior energy storage capacity, extended service life, lighter construction, and immunity to the memory effect. Despite these benefits, their performance is heavily influenced by thermal conditions. Lithium-ion batteries require a tightly controlled thermal environment, ideally operating within a 15°C to 35°C range. Furthermore, in battery packs consisting of multiple cells, the temperature fluctuations across the modules must remain within a 5°C threshold to ensure safe and effective performance [2]. Multiple factors related to battery safety can contribute to the gradual decline in both the lifespan and performance of lithium-ion batteries. These include diminished efficiency caused by slow electrochemical reactions in cold environments, overheating due to high surrounding temperatures which lead to reduced capacity, and issues like electrical imbalance or spontaneous discharge over time [3]. Maintaining a consistent temperature across the battery pack is crucial to avoid the risk of thermal runaway and its potentially hazardous consequences. As such, implementing an effective thermal management strategy is essential to ensure the stability and reliability of battery systems [4].

Wang et al. [5] highlight the critical need for a robust battery thermal management system (BTMS) to improve the overall efficiency and reliability of electric vehicles. As the number of battery cells and their energy density increase, so does the internal heat generation, necessitating effective temperature control mechanisms. The research underscores the importance of designing a battery cooling system that can counteract the negative consequences of excessive thermal buildup, which poses both performance and safety concerns. A well-functioning BTMS is responsible for sustaining the battery within an optimal temperature window extracting heat during hot conditions, supplying warmth in colder environments, and ensuring even temperature distribution through proper insulation across all cells. Various methodologies have been employed to achieve this, leading to the categorization of BTMSs based on cooling medium (such as air, liquid, or solid-state phase change materials, the PCMs) [6], thermal process [7], energy input method, and whether the system makes direct or indirect contact with battery cells [8].

Comparative studies have shown that passive cooling systems using PCMs outperform forced-air active systems, especially under high ambient temperatures and during rapid discharging scenarios [9]. Nonetheless, Ling et al. [10] point out that relying solely on phase change materials (PCMs) is insufficient for sustained BTMS operation, as these materials eventually undergo full phase transition at elevated temperatures, losing their cooling capacity. Vapor compression systems, though widely used and relatively easy to design, face limitations in overall performance. These systems often rely on single-phase coolants with low thermal conductivity like water and require multiple heat exchangers, leading to increased size, weight, energy consumption, and cost. To address these drawbacks, Jin et al. [11] introduced a thermal regulation approach using a liquid cold plate, praised for its compact structure, high effectiveness, and ease of integration. Indirect liquid-based cooling has proven to outperform air-based systems when managing the intense heat generated by EV battery modules. Liquid-cooled BTMSs offer superior heat removal capabilities and operate more quietly, though they tend to be bulkier and more energy-intensive [12-13]. In contrast, air-cooling systems are lighter, less expensive, and mechanically simpler, with more compact designs [14-15].

In the current work, we have carried out CFD simulations for the analysis of the air-cooled battery thermal management system. For this, a battery pack is under consideration which has four cells in each row along the air flow direction.

2. PROBLEM STATEMENT

In our work, we will perform numerical simulations for thermal management of battery pack using computational fluid dynamics techniques. For reducing the computational cost, we take advantage of the symmetry in the geometry, and hence we took only a half row of the batteries and the associated air passage for its cooling, as may be seen in Figure 1. Thus, the computational domain comprises cell bodies and a fluid body with inlet-outlet arrangement. There are four 18650 li-battery cells in a row along the flow direction, which means that each battery cell is cylindrical and has 18 mm diameter (or 9 mm radius) and 65 mm height. Due to the use of symmetry, half of the batteries are included in the computational domain. The inlet dimensions are 11.5 mm width and 65 mm height, which means that near the battery cells, there is a 2.5 mm space for the air passage, while height of the inlet is same as of the cell height. The distance between the inlet and the first cell is 70 mm and same is the distance between last cell and the outlet. The gap between two consecutive cells is 5 mm. The heat source is the heat generation rate of 4,20,0000 W/m^3 inside each cell. Following are the thermo-physical properties of the lithium-ion cell and the air.

Table 1. Thermo-physical properties of the lithium-ion cell.

Property	Value	Unit
Density	2092	Kg/m^3
Specific heat	678	J/(Kg-K)
Thermal conductivity	18.2	W/(m-k)

Table 2. Thermo-physical properties of the air.

Property	Value	Unit
Density	1.225	Kg/m^3
Specific heat	1006.43	J/(Kg-K)
Thermal conductivity	0.0242	W/(m-k)
Viscosity	1.7894e^{-05}	Kg/(m-s)

Following is the computational domain, that contains a half row of the cells in the battery pack along with the associated air passage.

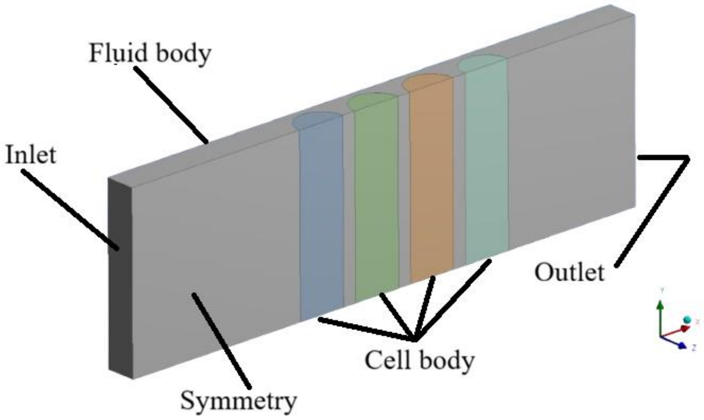

Figure 1. Computational domain containing fluid and solid bodies.

3. MATHEMATICAL FORMULATION

In this section, we give some flow and heat transfer assumptions and the governing equations of the problem.

3.1 Flow and Heat Transfer Assumptions

(a) The problem under consideration is a 3D, turbulent, incompressible and steady state problem.
(b) The battery cells are placed in the air passage with inlet-outlet arrangement.
(c) The thermo-physical properties of the air are constant because of the incompressible flow.
(d) At the solid-liquid interface, the heat transfers through the relation $k_{cell}\frac{\partial T_{cell}}{\partial n}=k_{air}\frac{\partial T_{air}}{\partial n}$.

3.2 Mathematical Model

The flow model comprises the Navier-Stokes equations along with the continuity and energy equations. The complete flow model is given as under.

The mathematical model that governs the flow is

$$\nabla\cdot u=0, \tag{1}$$

$$\rho(u\cdot\nabla)u=-\nabla p+\mu\nabla^2 u+\rho g+S_u, \tag{2}$$

$$\rho c_p(u\cdot\nabla T)=\lambda\nabla^2 T+S_T, \tag{3}$$

where u, g and p are the velocity vector, gravitational acceleration and pressure respectively. T is the temperature, c_p is specific heat capacity and λ is the thermal conductivity.

For turbulence modeling, two additional transport equations of Standard $k-\varepsilon$ model are solved along with the flow model given above. These equations are given below.

$$\rho(u\cdot\nabla k)=\nabla\cdot\left[\left(\mu+\frac{\mu_t}{\sigma_k}\right)\nabla k\right]+P_k-\rho\varepsilon, \tag{4}$$

$$\rho(u\cdot\nabla\varepsilon)=\nabla\cdot\left[\left(\mu+\frac{\mu_t}{\sigma_\varepsilon}\right)\nabla\varepsilon\right]+C_{1\varepsilon}\frac{\varepsilon}{k}P_k-C_{2\varepsilon}\rho\frac{\varepsilon^2}{k}, \tag{5}$$

where k is the turbulent kinetic energy, ε is the turbulent dissipation rate, and turbulent viscosity relation is given by

$$\mu_t=\rho C_\mu\frac{k}{\varepsilon}. \tag{6}$$

3.3 Heat Transfer Coefficient

The heat transfer coefficient h is defined as

$$h=\frac{q}{A\cdot\Delta T},$$

where q is the uniform heat flux, A is the surface area exposed to the fluid, and ΔT is the temperature difference between the solid surface and the ambient fluid.

3.4 Boundary Conditions

The inlet boundary is set to velocity inlet, while the velocity varies from 1 m/s to 5 m/s for the parametric study. The outlet boundary is set to pressure outlet with zero-gauge pressure. All other boundaries are set to symmetry boundary condition in order take advantage of symmetry and to avoid wall complexities wherever applicable. Mathematically, the symmetry boundary condition is defined as $\frac{\partial T}{\partial n}=0$. The temperature of the air entering through the inlet is 300 K.

4. MESHING

In order to use the Finite Volume Method, the computational domain must be discretized into smaller volumes. In our computational mesh, there are 39938 nodes and 122004 elements with max skewness of 0.88281. The skewness less than 0.9 ensures the accuracy of the results. An isometric view of the computational mesh is shown in Figure 2. The mesh of the computational domain is unstructured mesh, and it is conformal mesh which means that the solid and fluid bodies share nodes, edges and the faces at the interface to avoid mesh complexities. The mesh is body fitted at the fluid-solid interfaces. We have added inflation layers also which are body fitted cells to capture the boundary layer impact properly.

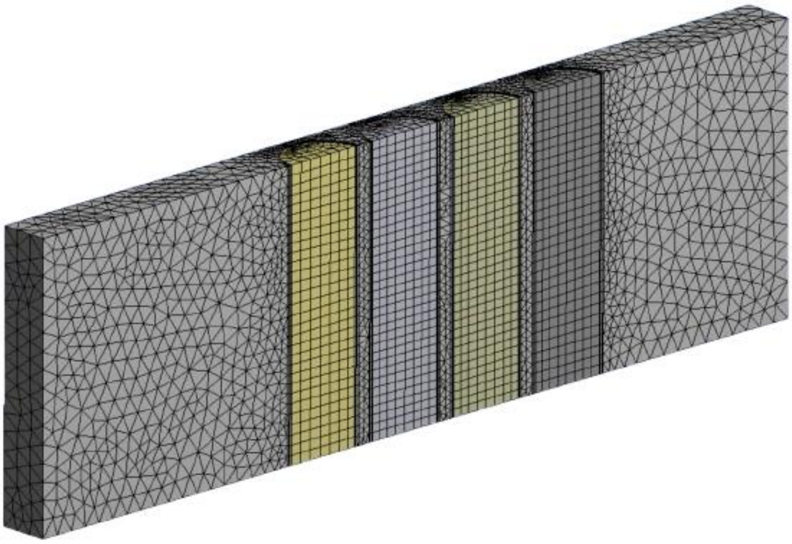

Figure 2. Mesh of the computational domain.

5. SOLUTION PROCEDURE

We solve the flow problem numerically using Finite Volume Method which is built-in in ANSYS Fluent 16.2. All the tasks of the simulations, i.e., geometry creation, meshing, choice of models, solution and postprocessing have been performed using ANSYS. For solution, SIMPLE scheme is used for the pressure-velocity coupling. For spatial discretization, the Green-Gauss Cell-Based method is used for the gradient calculations, second order interpolation is used for the pressure for enhanced accuracy in the pressure-velocity coupling, and second order upwind scheme is used for the momentum and energy equations. The threshold for the residuals is set to below 10^{-3} for continuity, momentum and turbulence model equations while it is 10^{-6} for the energy equation. The calculations are performed unless the convergence of the procedure to the required accuracy.

6. RESULTS AND DISCUSSION

In this section, we discuss in detail the influence of the inlet velocity on the inlet pressure, cell temperature and the heat transfer coefficient.

6.1 Steady Thermal Parametric Analysis

In this subsection, we discuss the behavior of some important parameters with respect to the increasing velocity.

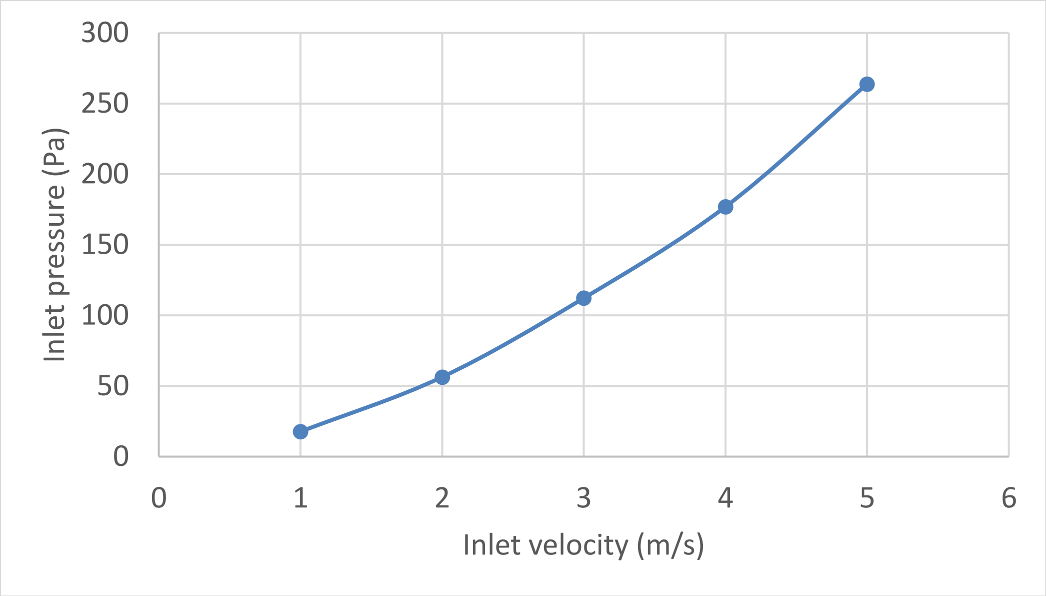

Figure 3. Pressure vs inlet velocity

In Figure 3, the relationship between the velocity and the pressure given. The *x*-axis displays the inlet velocity, increasing from 1 m/s to 5 m/s, while the *y*-axis shows the corresponding computed pressure values, ranging from 17.67 to 263.81 Pa. From the plotted data points and the connecting curve, it is evident that as the velocity increases, the pressure increases at an accelerating rate. There is a nonlinear relationship, likely quadratic, between the two variables. The curve starts relatively shallow and steepens progressively, signifying that small increases in velocity at higher values result in much larger increase in pressure. This pattern is typical in fluid dynamics and aerodynamics, where pressure is often proportional to the square of the velocity, as described by Bernoulli's principle or the dynamic pressure formula $P = \frac{1}{2}\rho v^2$, where P is the pressure, ρ is the fluid density, and v is the velocity. Although fluid density is not given in this graph, the curve aligns with this theoretical model. The graph contains markers at each data point which shows a significant rise in pressure, highlighting a rapid acceleration in pressure growth as velocity climbs.

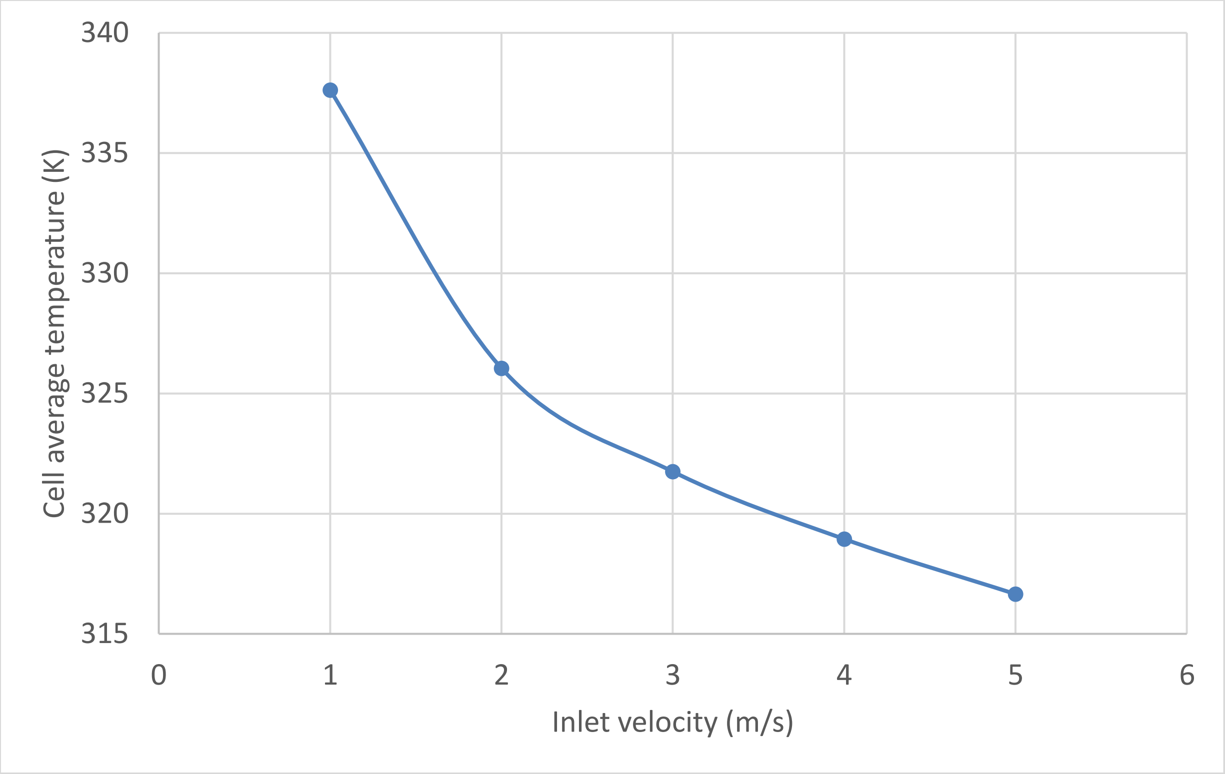

Figure 4. Average cell temperature and Velocity

The chart in Figure 4 showcases how cell temperature changes with respect to the inlet velocity, showing a clear inverse relationship between fluid velocity and average cell temperature. As the velocity of the air increases from 1 meter per second to 5 meters per second, the temperature of the cell steadily decreases. At the starting point of velocity of 1 m/s, the temperature is the highest, measuring approximately 338 K. As the velocity doubles to 2 m/s, a noticeable decline in the temperature occurs, dropping to around 326 K. This downward trend continues as the air speed rises, with the temperature reaching close to 316 K at the highest measured velocity of 5 m/s. The pattern shown in the graph indicates that increasing velocity contributes to enhanced cooling performance. When air moves over a heated surface more rapidly, it is able to extract heat more efficiently. At lower velocities, heat tends to accumulate due to slower thermal removal, leading to higher operating temperatures. As the flow intensifies, thermal energy is transferred away from the surface at a faster rate, reducing the system's internal temperature.

It is to be noted that the rate of temperature decrease is sharper at lower speeds and becomes more gradual at higher velocities. This reflects a condition of diminishing thermal benefit; early increases in velocity causes significant cooling, but additional gains become less impactful as flow rate continues to rise.

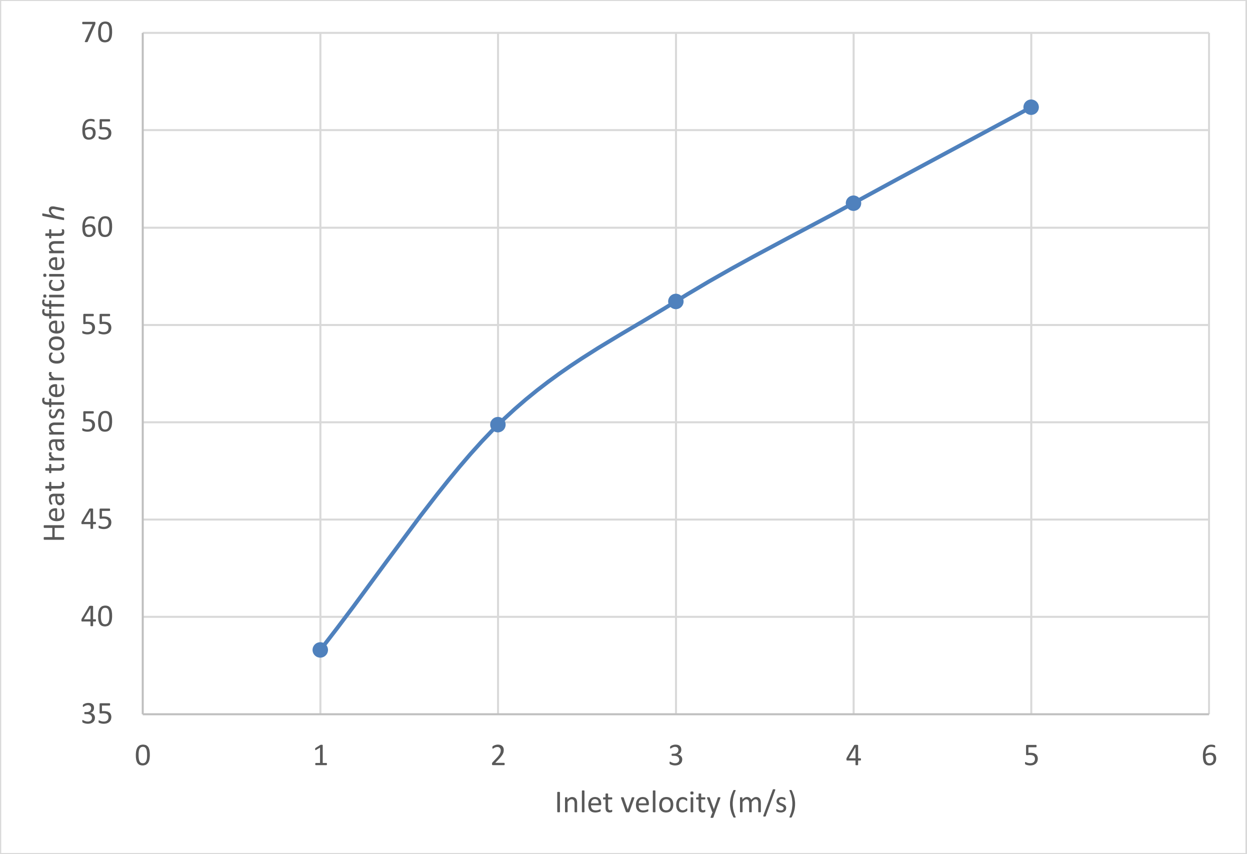

Figure 5. Heat transfer coefficient at cell surface vs velocity.

In Figure 5, heat transfer coefficient is plotted against the inlet velocity. The graph shows that the heat transfer coefficient increases with the velocity from approximately 38 to 66 W/m²·K**.** This trend is expected and aligns with convective heat transfer theory, where higher fluid velocities enhance the convective exchange between the fluid and the solid surface. The behavior is consistent with average cell temperature in Figure 4, which means that higher the convective heat implies the rapid temperature decline of the hot body.

6.2 Spatial Thermal and Flow Analysis: Contour Analysis

In this subsection, we give detailed local analysis of behavior of the field variables for the case when inlet velocity is 5 m/s.

In Figure 6, contour plot of the pressure at the central horizontal plane is given.

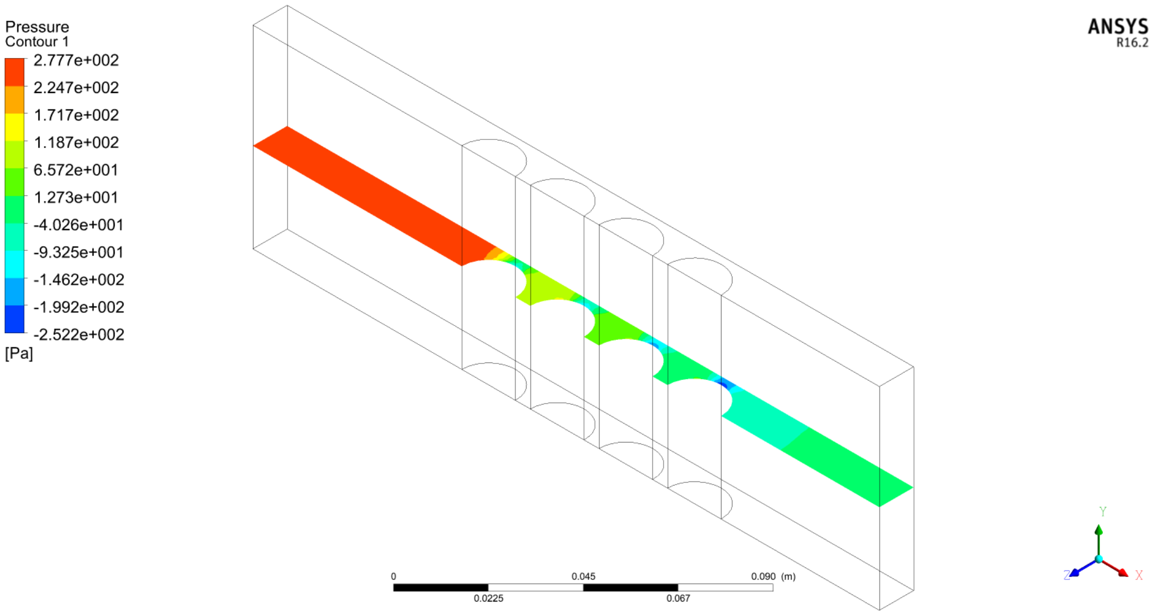

Figure 6. Contours plot of static pressure at the central horizontal plane.

For inlet velocity of 5 m/s at the inlet, pressure is computed which is around 277.7 Pa at the inlet. The contours in Figure 6 reveals the pressure distribution across the rectangular duct with four cylindrical batteries placed at regular intervals. We can see that the pressure reduces downstream, and it is zero gauge at the outlet and it is the outlet boundary condition. Near the battery cells, the color is blue indicating negative gauge pressure near the battery cells because of too narrow passage for the air. In this area, the velocity of the air is maximum and the pressure is the minimum. The wake zones that form behind each cylinder further reduce pressure levels, as flow separation and turbulence take place in these regions. These wake zones can be seen as regions of lower pressure trailing behind the cylindrical cells. The presence of battery cells alters the natural streamline flow, creating drag and flow disturbances which directly influence the pressure field.

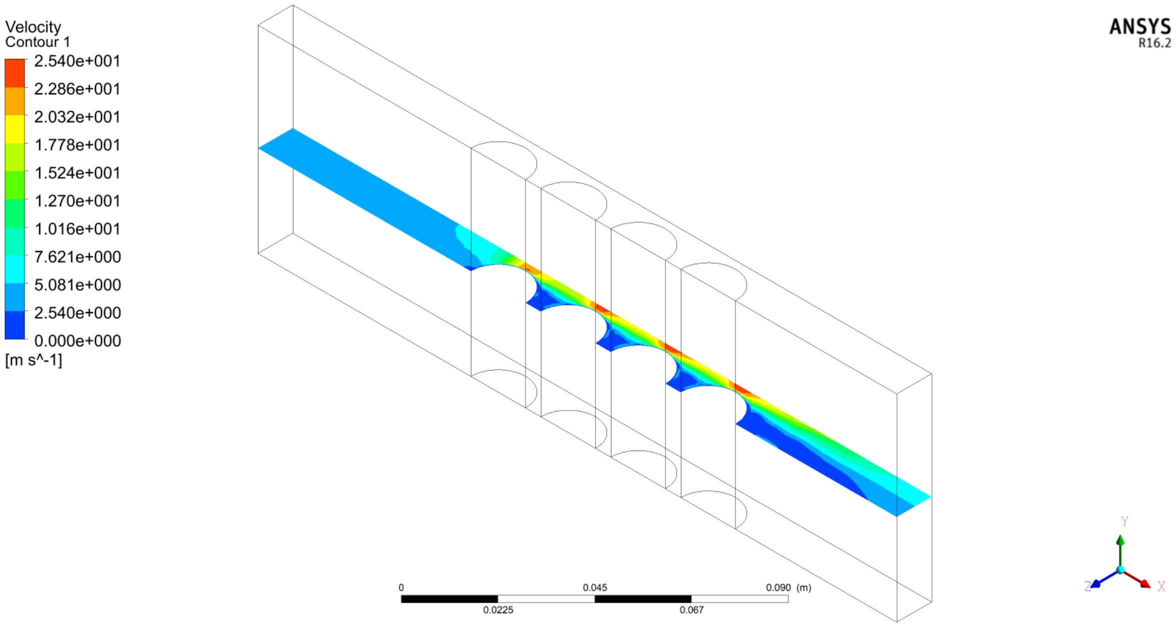

Figure 7. Contours plot of velocity at the central horizontal plane.

In Figure 7, contour plot of the velocity is given. It is clear from the figure, that the velocity at the inlet is 5 m/s. As the air reaches the first cell, the air has to rush towards the narrow path present near the cell bodies, and as a result, the velocity of the fluid rises to its peak to maintain the flow. If we see the pressure and velocity contours combinedly in Figures 6 and 7, it can be observed that the velocity is highest in the regions where the gauge pressure is least. Moreover, due to the flow separation near the cell bodies, the pockets are formed in the space between the battery cells. Thus, there is negligible flow, and this is the reason, the temperature in these pockets is higher, as may be seen in Figure 8. The temperature of the air in the air passage is found to be minimum.

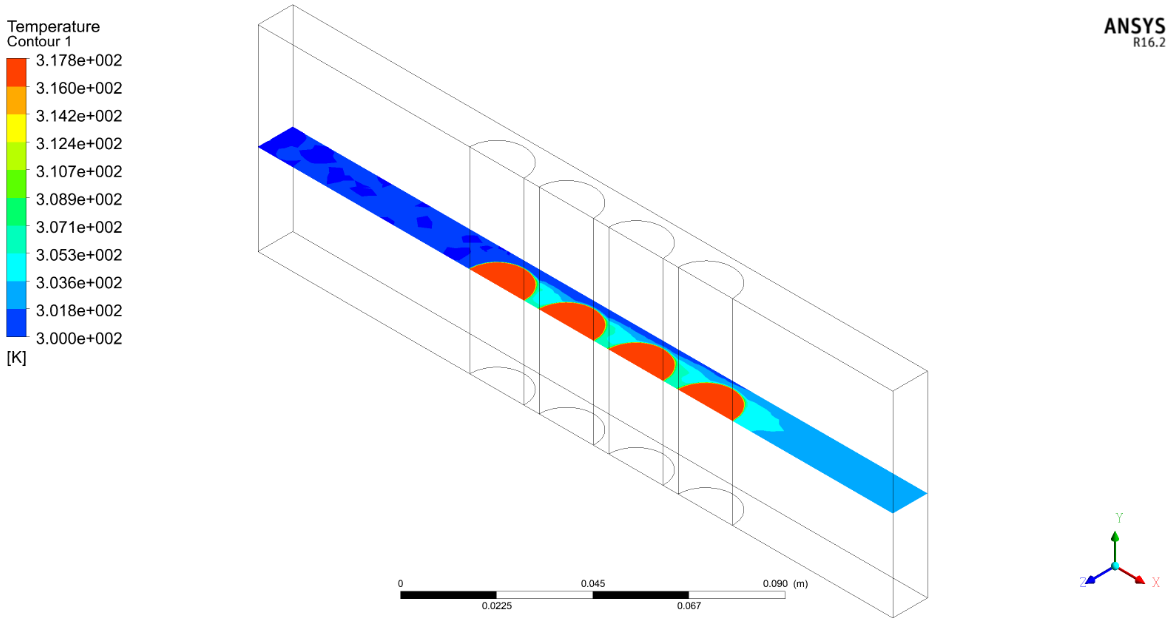

Figure 8. Contours plot of temperature at the central horizontal plane.

In Figure 8, contour plot of the temperature is given. The color bar on the left defines temperature levels in Kelvin (K), ranging from 300 K (dark blue) to 317.3 K (red). This range indicates the variation in temperature from the inlet air temperature to the hottest zones on the surface of the battery cells. Red zones visible around the mid-sections of the battery cells indicate the regions of high thermal intensity and this is because of the heat generation rate within the battery cells, reaching up to approximately 317 K (44°C). The positioning of the red spots aligns with expected thermal accumulation, especially when cells are discharging or charging under load.

Each battery shows a localized red or orange semicircle, revealing the point of maximum surface temperature where the flow first contacts the heated battery surface. These hot spots emphasize the critical need for sufficient convective heat transfer to maintain battery safety and efficiency.

The temperature at the inlet is 300 K, colored as dark blue. This confirms that the air entering the channel is initially cool and capable of absorbing heat. As it progresses through the channel and past the heat-generating cells, the temperature of the air rises, shown by the shift from blue to cyan and green. Notably, the region immediately behind each battery cell, downstream wake zones, transitions back to blue shades. These zones exhibit lower temperatures, possibly due to reduced fluid contact or flow stagnation, which hinders heat exchange and may allow cooler air to accumulate in recirculation zones.

The temperature distribution along the midplane clearly illustrates how the cooling air absorbs heat from each battery in the sequence. The gradual increase in air temperature (from left to right) indicates that heat is being transferred effectively, but also warns of reduced thermal capacity of the air further downstream.

This result highlights the importance of:

- airflow distribution pattern to ensure all cells receive adequate cooling.
- cell spacing and orientation to avoid hot spots and thermal buildup.
- inlet air temperature and flow rate optimization to enhance overall heat removal.

7. CONCLUSIONS

The following are the findings in the study.

1. The inlet pressure increases with the increase in the inlet velocity,
2. The temperature of the fluid decreases with an increase in the inlet velocity, because fast moving fluid is more capable of carrying the heat,
3. The temperature of the cells is reduced with increase in the inlet velocity,
4. The heat transfer coefficient increases with increase in the inlet velocity

REFERENCES

[1] Dinçer I, Hamut H S and Yildiz N J 2017 Thermal Management of Electric Vehicle Battery Systems (John Wiley & Sons Ltd)

[2] Pesaran AA., Santhanagopalan S, Kim GH. Addressing the impact of temperature extremes on large format li-ion batteries for vehicle applications (presentation). No. NREL/PR-5400- 58145. National Renewable Energy Lab.(NREL), Golden, CO (United States), 2013.

[3] Bandhauer TM, Garimella S, Fuller TF. A critical review of thermal issues in lithium-ion batteries. Electrochemical Society 2011;158:R1-25.

[4] Wang Q, Ping P, Zhao X., Chu G, Sun J, Chen C. Thermal runaway caused fire and explosion of lithium-ion battery. power sources 2012;208:210-24.

[5] Wang Q, Jiang, B, Li B, Yan Y. A critical review of thermal management models and solutions of lithium-ion batteries for the development of pure electric vehicles. Renewable and Sustainable Energy Reviews 2016;64:106-28.

[6] Rao Z, Wang S. A review of power battery thermal energy management. Renewable and Sustainable Energy Reviews 2011;15:4554-71.

[7] J. Kim, J. Oh, H. Lee, Review on Battery Thermal Management System for Electric Vehicles, Applied Thermal Engineering (2018)

[8] H. Teng, K. Yeow, Design of direct and indirect liquid cooling systems for high capacity, high-power lithium-ion battery packs. Alternative Powertrains 2012;1(2012-01-2017):525-36.

[9] R. Sabbah, R. Kizilel, J. Selman, S. Al-Hallaj, Active (air-cooled) vs. passive (phase change material) thermal management of high-power lithium-ion packs: Limitation of temperature rise and uniformity of temperature distribution, J Power Sources 2008;182:630–8.

[10] Ling Z, Wang F, Fang, X, Gao X, Zhang Z. A hybrid thermal management system for lithium-ion batteries combining phase change materials with forced-air cooling. Applied Energy 2015;148:403-9

[11] Jin L, Lee P, Kong X, Fan Y, Chou S. Ultra-thin Mini channel LCP for EV battery thermal management. Appl Energy 2014;113:1786–94.

[12] R. Koyama, Y. Arai, Y. Yamauchi, S. Takeya, F. Endo, A. Hotta, R. Ohmura, Thermophysical properties of trimethylolethane (TME) hydrate as phase change material for cooling lithium-ion battery in electric vehicle, J. Power Sources 427 (2019) 70-76.

[13] M. Arasu, Q. Ahmed, G. Rizzoni, Optimizing Battery Cooling System for a Range Extended Electric Truck, SAE Technical Paper, 0148-719, 2019.

[14] M.H. Westbrook, M. Westbrook, The Electric car: Development and Future of Battery, Hybrid and Fuel-Cell Cars, Iet 38, 2001.

[15] M.K. Subramani, S. Mohan, T. Subramani, A. Sathishkumar and S.C. Kim, Thermal Performance Optimization of Air-Cooled Battery Packs in Electric Vehicles: An Integrated CFD and Machine-Learning Approach, International Journal of Thermophysics, 47:50, 2026.